The Astrophysical Journal, 926:97 (14pp), 2022 February 10 https://doi.org/10.3847/1538-4357/ac4158

Physical Regimes of Two-dimensional MHD Turbulent Reconnection in Different Lundquist Numbers

Haomin Sun[1,2], Yan Yang[3,4], Quanming Lu[1,2], San Lu[1,2], Minping Wan[3], and Rongsheng Wang[1,2]
[1] CAS Key Laboratory of Geospace Environment, Department of Geophysics and Planetary Science, University of Science and Technology of China, Hefei, Anhui, People's Republic of China; qmlu@ustc.edu.cn
[2] CAS Center for Excellence in Comparative Planetology, People's Republic of China
[3] Southern University of Science and Technology, Shenzhen, Guangdong 518055, People's Republic of China; yanyangpku@gmail.com
[4] University of Delaware, Newark, DE 19716, USA
Received 2021 August 31; revised 2021 November 20; accepted 2021 December 6; published 2022 February 16

Abstract

Using two-dimensional MHD simulations in different Lundquist numbers S, we investigate physical regimes of turbulent reconnection and the role of turbulence in enhancing the reconnection rate. Turbulence is externally injected into the system with varying strength. Externally driven turbulence contributes to the conversion of magnetic energy to kinetic energy flowing out of the reconnection site and thus enhances the reconnection rate. The plasmoids formed in high Lundquist numbers contribute to the fast reconnection rate, as well. Moreover, an analysis of the power of turbulence implies its possible association with the generation of plasmoids. Additionally, the presence of turbulence has great impact on the magnetic energy conversion and may be impactful also for the Kelvin–Helmholtz instability in the magnetic reconnection process.

Unified Astronomy Thesaurus concepts: Solar magnetic reconnection (1504); Solar magnetic fields (1503); Solar physics (1476); Magnetic fields (994); Astrophysical magnetism (102); Plasma physics (2089); Interstellar magnetic fields (845); Burst astrophysics (187); Plasma astrophysics (1261); Magnetohydrodynamics (1964); Interplanetary magnetic fields (824)

1. Introduction

Magnetic reconnection is one of the most fundamental plasma physics processes (Dungey 1953; Sweet 1958; Parker 1973; Drake et al. 2006), that occurs in a wide range of applications in laboratory, space, and astrophysical plasmas, including the Earth's and planetary magnetosphere (Øieroset et al. 2002; Nagai et al. 2003; Egedal et al. 2005), solar flares (Parker 1957; Sweet 1958; Ciaravella & Raymond 2008; Liu et al. 2008; Su et al. 2013), solar wind (Gosling 2007; Osman et al. 2014), nuclear fusion devices (Yamada et al. 1994; Ono et al. 2015), and high-energy-density explosive events (Zweibel & Yamada 2009; Uzdensky 2011). The reconnection process is accompanied by the topology changing of magnetic field lines, which is featured by two oppositely directed field lines breaking up and reorganizing. While kinetic effects must be considered at very small scales, the magnetohydrodynamic (MHD) model remains a credible description for magnetic reconnection as the resistive layer is much larger than the ion kinetic scale. By using single-fluid MHD analysis, the pioneering works in Sweet (1958) and Parker (1957) established the Sweet–Parker (SP) reconnection model, which yields reconnection rates scaled as $S^{-1/2}$ ($S = 2v_A L/\eta$ is the Lundquist number, where v_A is the Alfvén speed, L is the half length of the current sheet, and η is the resistivity). Since the Lundquist number S is typically large in the universe (e.g., $S \sim 10^{14}$ in solar flares, $\sim 10^{18}$ in the interstellar media), the predicted reconnection rate by the SP model falls well below that measured in observations (Sonnerup 1974; Yokoyama et al. 2001; Liu et al. 2008; Takasao et al. 2012; Su et al. 2013). The inadequacy of the SP model has led to the realization of fast reconnection models that accommodate more sophisticated physics. One direct modification to the SP model was proposed by Petschek (1964), which was controversial because the origin of shocks in the theory was unclear (Biskamp 1986; Uzdensky & Kulsrud 2000).

A different approach to speed up the reconnection rate is turbulent reconnection involving the diffusion of magnetic fields (Hesse & Schindler 1988; Lazarian & Vishniac 1999, hereafter LV99; Eyink 2015; Lazarian et al. 2015). In the highly influential LV99 model, the authors took into account the small-scale magnetic field structures in the turbulence, which results in a fast reconnection rate and is confirmed in numerical simulations (Kowal et al. 2009, 2012; Yang et al. 2020) and observations (Sych et al. 2009). Note that the LV99 model, on the basis of the turbulent scaling law given by Goldreich & Sridhar (1995), is intrinsically three-dimensional. Another theoretical model is related to the plasmoid instability, which generates plasmoids within a current sheet (Lapenta 2008; Cassak et al. 2009; Bhattacharjee et al. 2009; Samtaney et al. 2009; Huang & Bhattacharjee 2010, 2013; Uzdensky et al. 2010; Loureiro et al. 2012; Loureiro & Uzdensky 2016). It has been found that when the Lundquist number S is greater than a critical value $S_c \sim 10^4$, the current sheet is vulnerable to plasmoids and a plasmoid chain can be observed (Loureiro et al. 2007; Bhattacharjee et al. 2009). Both two-dimensional and three-dimensional simulations (Loureiro et al. 2005, 2012; Samtaney et al. 2009; Huang & Bhattacharjee 2010, 2013, 2016; Uzdensky et al. 2010) have demonstrated that the plasmoid instability and consequent interactions between the generated plasmoids lead to enhancement of the reconnection rate over the SP reconnection rate, which is nearly independent of the high enough Lundquist number S. An even more drastic enhancement of the reconnection rate can be observed when the thickness of current sheets approaches the ion inertial length, where kinetic effects become

dominant (Daughton et al. 2009; Yamada et al. 2010 and references therein). Karimabadi & Lazarian (2013) made a systematic review of different models of turbulent reconnection, highlighting their differences, such as three-dimensional models that rely on turbulent broadening of the layer, two-dimensional MHD models that rely on thinning of the current sheet due to plasmoid instability and collisionless models due to the predominance of kinetic effects. Depending on the astrophysical conditions, different fast reconnection models, each having their own adherents, might be applicable and dominant.

The plasma environment in most interstellar media and solar atmosphere has a high Reynolds number and therefore is usually turbulent (Pope 2004). The interplay between turbulence and magnetic reconnection is of great interest. Reconnection can self-generate turbulence (Che et al. 2011; Daughton et al. 2011; Karimabadi et al. 2013; Beresnyak 2016; Huang & Bhattacharjee 2016; Kowal et al. 2017; Pucci et al. 2018). Also, there has been significant progress in understanding reconnection occurring in a turbulent medium. Both satellite observations (Retinò et al. 2007; Sundkvist et al. 2007; Wang et al. 2016; Yordanova et al. 2016; Vörös et al. 2017; Phan et al. 2018; Stawarz et al. 2019) and numerical simulations (Servidio et al. 2009, 2010; Daughton et al. 2014; Franci et al. 2017; Haggerty et al. 2017; Shay et al. 2018) have supported that the magnetic reconnection is an important mechanism responsible for the dissipation of turbulent energy and the subsequent heating of the solar corona and solar wind. Alternatively, a number of earlier studies imposed external turbulent fluctuations within magnetic reconnection in an attempt to understand how it affects reconnection, which was addressed in Matthaeus & Lamkin (1985), Matthaeus & Lamkin (1986), Fan et al. (2004), Loureiro et al. (2009), and Kulpa-Dybeł et al. (2010) for two-dimensional cases; in Smith et al. (2004) for two-and-half-dimensional cases; and in Kowal et al. (2009) for three-dimensional cases.

In this paper, we proceed with an incompressible setup in two-dimensions in the presence of turbulence. Note that space plasmas, e.g., in the solar corona, the solar wind, and the Earth's magnetosheath, show variability in various characteristic parameters such as the plasma β (the ratio of thermal-to-magnetic pressure) and the corresponding compressibility. The compression effect was found to be important for reconnection and particle acceleration in low-β plasmas (Birn et al. 2012; Drury 2012; Zank et al. 2014; Provornikova et al. 2016; Montag et al. 2017; Li et al. 2018; Zenitani & Miyoshi 2020). Here we only consider incompressive effects (Drake et al. 2006), which are expected to be dominant in high-β regimes; see, for example, Chhiber et al. (2018), Eriksson et al. (2018), and Wang et al. (2021). Although the pure incompressible model does not take into account the compression effect, there are many aspects of incompressible cases and trends with parameters that could be applicable to compressible cases, as well. The closest studies to ours are Loureiro et al. (2009) and Kulpa-Dybeł et al. (2010), wherein Loureiro et al. (2009) focused on the role of plasmoids at high Lundquist numbers and Kulpa-Dybeł et al. (2010) studied the dependence of the reconnection rate on different quantities, including the power of turbulence and the uniform resistivity. Subsequent to their works, here we are concerned with the diagram for turbulent magnetic reconnection in different Lundquist numbers and how externally driven turbulence and plasmoids could mutually contribute to the enhancement of the reconnection rate. In particular, we present a detailed analysis of kinetic–magnetic energy exchange during magnetic reconnection based on a well-defined quantitative proxy.

This paper is organized as follows. The simulation model is described in Section 2, followed by the method to measure the reconnection rate in Section 3. The results are discussed in Section 4, where we present the global reconnection rate, the turbulent magnetic reconnection at small and large S, the kinetic–magnetic energy exchange process and the observed local configuration that may support the development of Kelvin–Helmholtz waves. The conclusions and discussion are given in Section 5.

2. Simulation Model

To study the effect of turbulence on the magnetic reconnection, we conduct direct numerical simulations of the incompressible two-dimensional MHD equations:

$$\frac{\partial \omega}{\partial t} + (\boldsymbol{v}\cdot\nabla)\omega = (\boldsymbol{B}\cdot\nabla)j + \nu\nabla^2\omega + f, \tag{1}$$

$$\frac{\partial \psi}{\partial t} + (\boldsymbol{v}\cdot\nabla)\psi = \eta\nabla^2\psi, \tag{2}$$

where $\boldsymbol{v}$, $\boldsymbol{B} = \nabla\psi\times\hat{\mathbf{z}}$, $\omega = (\nabla\times\boldsymbol{v})\cdot\hat{\mathbf{z}}$, ψ, $j = (\nabla\times\boldsymbol{B})\cdot\hat{\mathbf{z}} = -\nabla^2\psi$, ν, and η denote the velocity, the magnetic field, the vorticity, the magnetic potential, the current density, the kinematic viscosity, and the magnetic resistivity, respectively. A constant density $\rho = const$ is assumed, which is set to be 1 here. We have normalized B by $\sqrt{4\pi\rho}$. An externally imposed (turbulent) forcing $\boldsymbol{F}$ is applied to the momentum equation, which corresponds to $f = (\nabla\times\boldsymbol{F})\cdot\hat{\mathbf{z}}$ in Equation (1).

We numerically solve Equations (1)–(2) on a domain $[-\pi, \pi]\times[-\pi, \pi]$ with periodic boundary conditions in all directions using the standard pseudospectral method. The fields are advanced in time by a second-order Adam–Bashforth scheme. All runs discussed here are carried out using 4096^2 resolution. The convergence of our simulation cases has been tested by varying the spatial resolutions and time steps. The simulations are initialized by $\omega = 0$ and $\psi(x, y) = \psi_{\rm eq}(x) + \psi_{\rm pert}(x)\times\cos(ky)$ (as used in Loureiro et al. 2005), where $\psi_{\rm eq}(x) = \psi_0/\cosh^2(x)$ is a tearing-mode unstable equilibrium, $\psi_0 = 3\sqrt{3}/4$, $k = 1$, and $\psi_{\rm pert}(x)\times\cos(ky)$ is an initial perturbation to facilitate the formation of current sheet and reconnection. $\psi_{\rm pert}(x)$ is calculated by the boundary-layer approach of tearing-mode instability (Bellan 2004, pp. 360–378), which follows $\psi'_{\rm eq}(x)[\psi''_{\rm pert}(x) - k^2\psi_{\rm pert}(x)] = \psi'''_{\rm eq}(x)\psi_{\rm pert}(x)$. The amplitude of $\psi_{\rm pert}$ is set to be $0.03\psi_0$. The maximum value of the equilibrium magnetic field, $B_{y,\max} = (d\psi_{\rm eq}/dx)_{\max} = 1$, is taken to be the reference value of the magnetic field. We set the Alfvén speed $v_A = B_{y,\max} = 1$ as the dimension of velocity.

The force $\boldsymbol{F}(\boldsymbol{x}, t)$ ($f = (\nabla\times\boldsymbol{F})\cdot\hat{\mathbf{z}}$ in Equation (1)) imposed in the velocity field is realized in Fourier space by $\hat{\boldsymbol{F}}(\boldsymbol{k}, t) = f_0\boldsymbol{G}(\boldsymbol{k}, t) = (f_0 G_x, f_0 G_y)$, where f_0 is a parameter that controls the turbulence strength and G_x in the x direction and G_y in the y direction are complex numbers whose real and imaginary parts are independent random numbers following the standard normal distribution. Therefore, $\langle\hat{\boldsymbol{F}}\rangle = 0$, and $\langle\hat{F}_i(\boldsymbol{k}, t)\hat{F}^*_j(\boldsymbol{k}', t')\rangle = 2f_0^2\delta_{ij}\delta(\boldsymbol{k} - \boldsymbol{k}')\delta(t - t')$, where i and j can be x or y and $\langle\ldots\rangle$ is the ensemble average. Meanwhile, the

compressive part accounting for a half portion of the force is eliminated by $\hat{\boldsymbol{F}} - \boldsymbol{k}(\boldsymbol{k} \cdot \hat{\boldsymbol{F}})/k^2$, such that the force does not break the incompressible constraint. In every time step Δt, the velocity field at the wave-number vector $\boldsymbol{k}$ evolves from $\hat{\boldsymbol{v}}(\boldsymbol{k}, t)$ to $\hat{\boldsymbol{v}}(\boldsymbol{k}, t) + \hat{\boldsymbol{F}} - \boldsymbol{k}(\boldsymbol{k} \bullet \hat{\boldsymbol{F}})/k^2$ and the kinetic energy density evolves from $\langle \hat{\boldsymbol{v}} \bullet \hat{\boldsymbol{v}}^* \rangle/2$ to $\langle \hat{\boldsymbol{v}} \bullet \hat{\boldsymbol{v}}^* \rangle/2 + f_0^2$. In this paper, we fix the forcing wave number $k_t = 7$, injecting turbulent motions with the characteristic scale $l_t = \pi/k_t \approx 0.45$. Therefore, the externally driven turbulence strength is

$$\epsilon = \sum_{|\boldsymbol{k}|=k_t} \frac{f_0^2}{\Delta t}.$$

To ensure that the turbulence strength is independent of the time step, f_0 is proportional to $\sqrt{\Delta t}$. Note that the force term does not need to be applied in the beginning of simulations and all simulations are started without turbulent forcing. After linear and X-point collapse stages, the initial tearing mode evolves to form a thin SP current sheet between two large magnetic islands, i.e., a laminar SP configuration (Loureiro et al. 2005) by which the value of ψ at ($x = 0$, $y = 0$) point (X-point) is $\psi_{00} \approx 0.45$ and the length of the current sheet is $2L \approx 0.8$. Therefore, the Lundquist number is defined by $S = 2v_A L/\eta \approx 0.8/\eta$. We use this laminar SP configuration as a starting point to switch on the turbulent forcing. Since then, the turbulence is continually injected.

In this paper, equal viscosity and resistivity $\eta = \nu$ are used, i.e., the magnetic Prandtl number is set to unity. Meanwhile, η is uniform, which is different from the anomalous resistivity in Malyshkin et al. (2005). The series of runs are constructed with two control parameters, one as to varying turbulent strength ϵ from 0.0 to 0.1, and the other as to varying resistivity η from 5.25×10^{-4} to 2.25×10^{-5} (i.e., varying Lundquist numbers S from 1.5×10^3 to 3.6×10^4). Further details on the simulation parameters are listed in Table 1.

Table 1
Simulation Parameters: Magnetic Resistivity η, Lundquist Number S, and the Power of Injected Turbulence ϵ

Runs	η	S	ϵ
A1	5.25×10^{-4}	1.52×10^3	0
A2	2.25×10^{-4}	3.56×10^3	0
A3	7.25×10^{-5}	1.10×10^4	0
A4	5.25×10^{-5}	1.52×10^4	0
A5	3.25×10^{-5}	2.46×10^4	0
A6	2.25×10^{-5}	3.56×10^4	0
B1	5.25×10^{-4}	1.52×10^3	0.01
B2	2.25×10^{-4}	3.56×10^3	0.01
B3	7.25×10^{-5}	1.10×10^4	0.01
B4	5.25×10^{-5}	1.52×10^4	0.01
B5	3.25×10^{-5}	2.46×10^4	0.01
B6	2.25×10^{-5}	3.56×10^4	0.01
C1	5.25×10^{-4}	1.52×10^3	0.03
C2	2.25×10^{-4}	3.56×10^3	0.03
C3	7.25×10^{-5}	1.10×10^4	0.03
C4	5.25×10^{-5}	1.52×10^4	0.03
C5	3.25×10^{-5}	2.46×10^4	0.03
C6	2.25×10^{-5}	3.56×10^4	0.03
D1	5.25×10^{-4}	1.52×10^3	0.05
D2	2.25×10^{-4}	3.56×10^3	0.05
D3	7.25×10^{-5}	1.10×10^4	0.05
D4	5.25×10^{-5}	1.52×10^4	0.05
D5	3.25×10^{-5}	2.46×10^4	0.05
D6	2.25×10^{-5}	3.56×10^4	0.05
E1	5.25×10^{-4}	1.52×10^3	0.1
E2	2.25×10^{-4}	3.56×10^3	0.1
E3	7.25×10^{-5}	1.10×10^4	0.1
E4	5.25×10^{-5}	1.52×10^4	0.1
E5	3.25×10^{-5}	2.46×10^4	0.1
E6	2.25×10^{-5}	3.56×10^4	0.1

3. Theoretical Reconnection Rate Measurement

While it is trivial to calculate the reconnection rate in laminar reconnection, caution is required in the presence of turbulence. The current sheet in a turbulent environment is strongly asymmetric (see Figures 1 and 3). It is natural to make use of the asymmetric Sweet–Parker equation (Cassak & Shay 2007) to estimate the instantaneous local reconnection rate of the current sheet:

$$E_{\mathrm{Local,theory}} \sim \sqrt{\frac{\eta v_{\mathrm{out}} B_1 B_2}{L}}, \tag{3}$$

where L is the half length of the current sheet, B_1 and B_2 are the upstream magnetic field on either side of the current sheet, and v_{out} is the outflow velocity of the current sheet. We employ the same methodology as those in Servidio et al. (2010) and Zhdankin et al. (2013), which will be explained in detail in Section 4, to identify the current sheet and the upstream and downstream regions. In this paper, the outflow speed v_{out} is taken to be the largest v_y in the two downstream regions, and B_1 and B_2 are taken to be the largest B_y on either side of the upstream regions. Only the y component is considered here since the corresponding x component is much smaller. One may recall that a "steady-state" assumption was made in the derivation of Equation (3) (Cassak & Shay 2007), under which the temporal derivatives in the MHD equations vanish. To firm up the assumption, we make a rough comparison between the time-derivative terms with other terms (see Appendix). The time derivatives in our cases are secular terms and nearly two orders of magnitude smaller than other terms, for which Equation (3) is justified physically when there is no plasmoids in the current sheet for our simulations.

To obtain the long time "global" reconnection rate, we perform a time average toward Equation (3), which yields

$$E_{\mathrm{Global,theory}} \sim \eta^{1/2} \left\langle \sqrt{\frac{v_{\mathrm{out}} B_1 B_2}{L}} \right\rangle, \tag{4}$$

where $\langle ... \rangle$ denotes the time average. Note that neither Equation (3) nor Equation (4) takes the effect of plasmoids into account. Their applicability for magnetic reconnection in the presence of plasmoids might therefore be deemed questionable.

4. Simulation Results

A first visual understanding of our setup can be seen in Figure 1, where we show the contour maps of out-of-plane current density for two characteristic runs, D2 and D3, at $t = 92$. The laminar SP configuration evolves under the effect of turbulent forcing. The two runs, with the same strength of turbulent forcing, differ in the Lundquist number. The presence of fluctuations and fine-scale structures is observable. In the zoomed-in subplots, one can see that plasmoids are generated

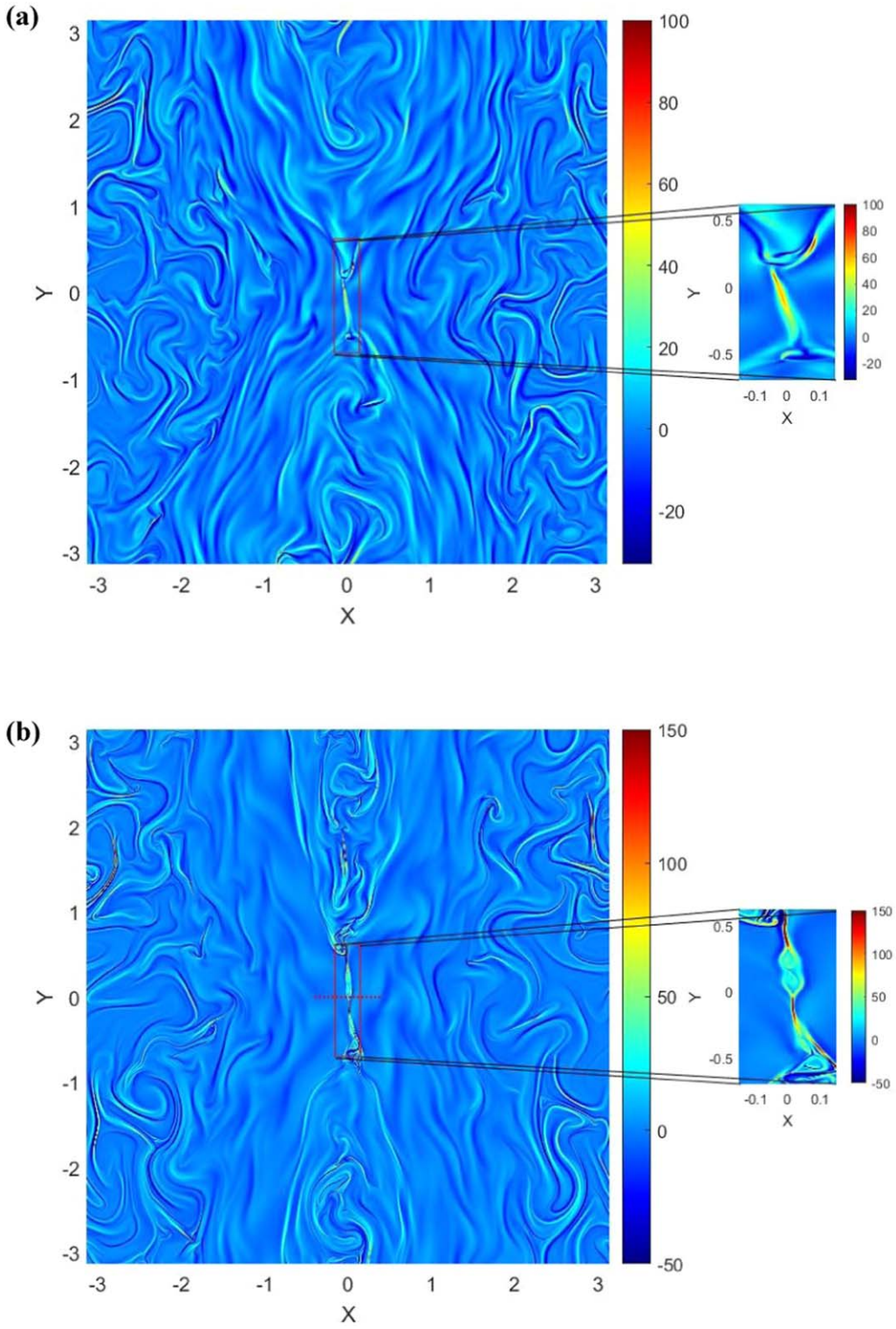

Figure 1. Contour maps of out-of-plane current density $\boldsymbol{J}$ at $t = 92$ for (a) Run D2 ($S = 3.56 \times 10^3$), without plasmoids in the current sheet and (b) Run D3 ($S = 1.10 \times 10^4$) with plasmoids in the current sheet. The regions in the red boxes are zoomed in to show the current sheet in more detail. The region over which we calculate the maximal value of ψ at each time step is indicated by the red dotted line in the middle of Figure 1(b).

in Run D3, while they are absent in Run D2. Our goal is to quantify and go deeper into the entangled dynamics when changing the Lundquist numbers and the turbulent strength. We shall take Runs D2 and D3 as examples in the following to contrast the diagram of magnetic reconnection at low and high Lundquist numbers.

4.1. Global Reconnection Rate

In the presence of plasmoids, the reconnection rate cannot be evaluated by the asymmetric Sweet–Parker equation, Equation (3), or Equation (4). Consequently, to get a rough idea of the reconnection rate for all simulations, we adopt the

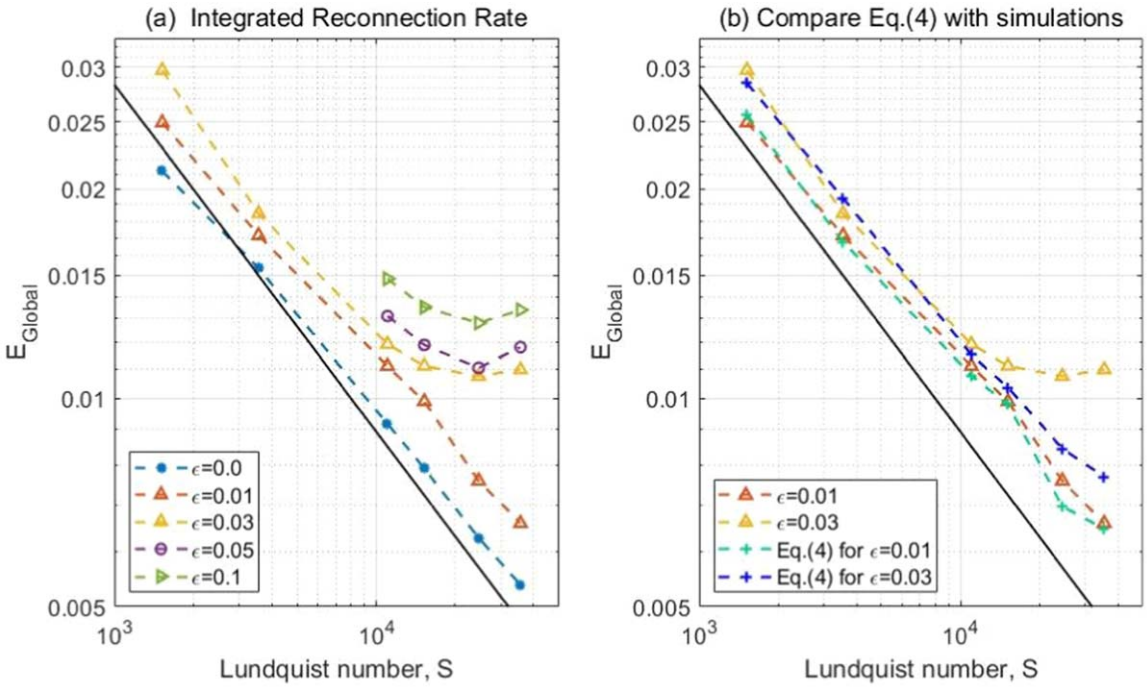

Figure 2. (a) Global reconnection rate estimated by the averaged value of $|d\psi_{\max}(t)/dt|$. Note that some simulations at small S with strong turbulence are not shown here since the current sheets tend to be destroyed by the turbulence such that the reconnection configuration no longer exists. (b) The estimation of the global reconnection rate by Equation (4) for the simulations with turbulent strength $\epsilon = 0.01$ and $\epsilon = 0.03$. The global reconnection rates for $\epsilon = 0.01$ and 0.03 marked by the orange and yellow lines with triangles are the same as those in (a). The estimation by Equation (4) (i.e., the green and blue curves) is in agreement with the averaged value of $|d\psi_{\max}(t)/dt|$ when S is small. However, it falls well below when S is large and turbulent forcing is strong. As a reference, the Sweet–Parker relation $E_{\rm global,Sweet-Parker} \sim \sqrt{2}\, v_{\rm out}^{3/2} v_A^{1/2} S^{-1/2}$ is indicated as a black solid line.

method as used in Loureiro et al. (2009). First, we obtain the time evolution of $\psi_{\max}(t)$, where $\psi_{\max}$ is the maximal ψ along the red dotted line shown in Figure 1. In all the simulations listed here, $\psi_{\max}(t)$ is a decreasing function of t (See Figure 5(a)). Second, we compute the absolute value of the slope of $\psi_{\max}$(t) (see Figure 5(b)). Finally, $|{\rm d}\psi_{\max}({\rm t})/{\rm dt}|$ is averaged over the time interval from $t - t_f = 15$ to $t - t_f = 45$, with t_f the time at which the turbulent forcing is switched on. The averaged value is taken to be an estimation of the global reconnection rate, shown in Figure 2(a). The reconnection rate based on the Sweet–Parker model $E_{\rm global,Sweet-Parker} \sim \sqrt{2}\, v_{\rm out}^{3/2} v_A^{1/2} S^{-1/2}$ is plotted as a reference. There are at least two points that we can make. First, the elevated reconnection rate at larger turbulence injection is observed. Second, the reconnection rate approximately scales as $S^{-1/2}$ at the small S range (e.g., $S < 10^4$). For higher S (e.g., $S > 10^4$), when turbulence injection is not that strong, the plasmoids may not generate in the current sheet region, thus the reconnection rate still scales as $S^{-1/2}$. At stronger turbulence injection, the reconnection rate asymptotes to finite values for high S, which has been previously published (Loureiro et al. 2009; Huang & Bhattacharjee 2010; Yang et al. 2020).

There is accumulating evidence of plasmoids that might be attributable to the enhanced reconnection rate at high S (Loureiro et al. 2005, 2012; Samtaney et al. 2009; Huang & Bhattacharjee 2010, 2013, 2016; Uzdensky et al. 2010). We show, however, that the reconnection rate can be enhanced, even when the plasmoids are absent at small S (see Figure 1(a)), which also merits attention. In Figure 2(b), we show the estimation of the global reconnection rate by Equation (4) at two turbulent strength levels. One can see that when $S < 10^4$, the asymmetric model Equation (4) gives a viable estimation, which still roughly scales as $S^{-1/2}$. Also noteworthy is that while Equation (4) remains valid at high S with the turbulent strength $\epsilon = 0.01$, it is incomplete at high S with $\epsilon = 0.03$, which is likely due to the presence of plasmoids. The results suggest a possible dependence of plasmoid generation on the turbulence strength which we present in more detail in the following.

4.2. Reconnection Regime in Small S

In this section, we concentrate on the reconnection regime when $S < 10^4$, which is illustrated in detail by one representative run, D2. Figure 3 shows the time evolution of current sheet for Run D2, where the turbulence is injected at $t \sim 52$. The current sheet is wavering around the central point, but no plasmoid is observed in the current sheet.

To take a closer look at the reconnection region, we employ the same methodology as those in Servidio et al. (2010) and Zhdankin et al. (2013) for identifying magnetic X-points and current sheet structures and characterizing them quantitatively in terms of their geometrical properties, such as width and length. Here we only give a brief review of the method and more details can be found in Servidio et al. (2010) and Zhdankin et al. (2013). To understand reconnection in two dimensions, we need to examine the topology of magnetic potential ψ in detail. According to $\nabla\psi = 0$, we can identify neutral points. If the Hessian matrix $H_{i,j}(\boldsymbol{x}) = \partial^2\psi/\partial x_i \partial x_j$ at the neutral point has both positive and negative eigenvalues, then the neutral point is a saddle point (X point). The geometry (direction, width, and length) of the current sheet and the upstream and downstream regions can also be obtained by the eigenvalues and eigenvectors of the Hessian matrix. In Figure 3(d), we show an example of an identified reconnection

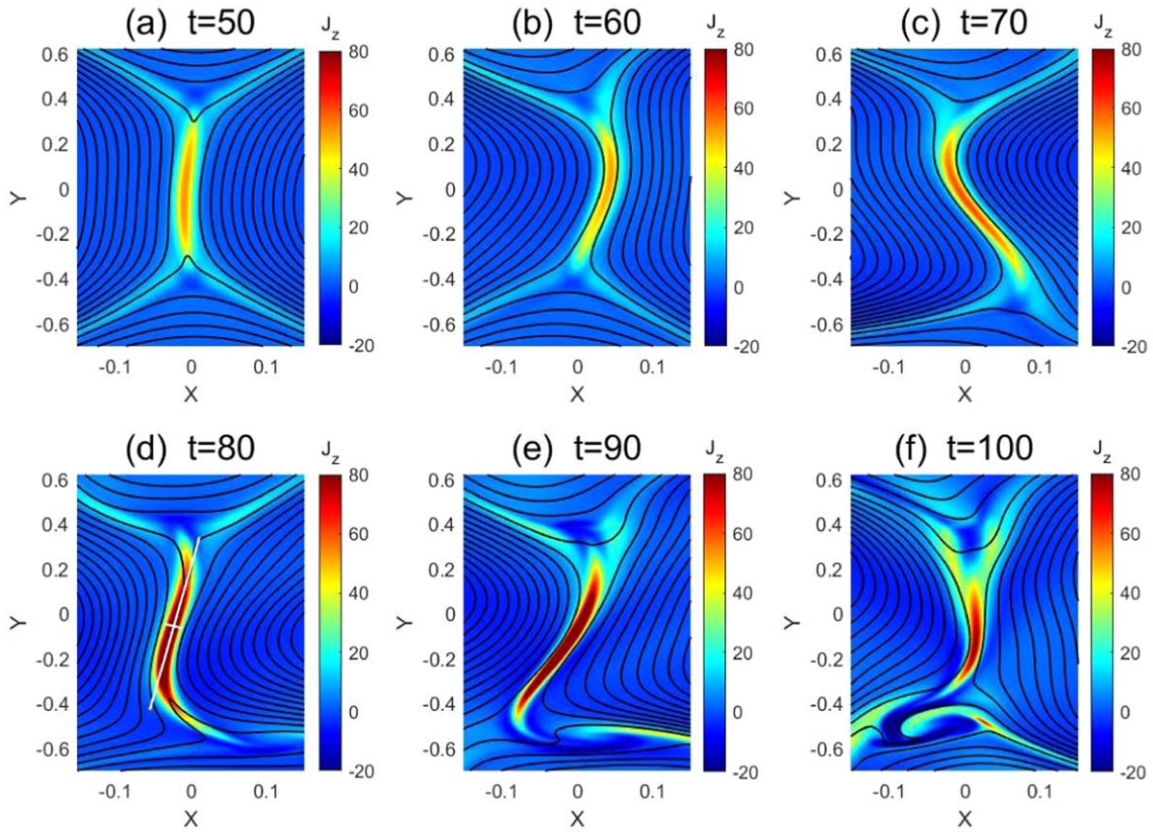

Figure 3. Configuration of current sheet together with contour lines (black solid lines) of magnetic potential for Run D2 at (a) $t = 50$, (b) $t = 60$, (c) $t = 70$, (d) $t = 80$, (e) $t = 90$, and (f) $t = 100$. The white cross in (d) indicates the width and length of the current sheet.

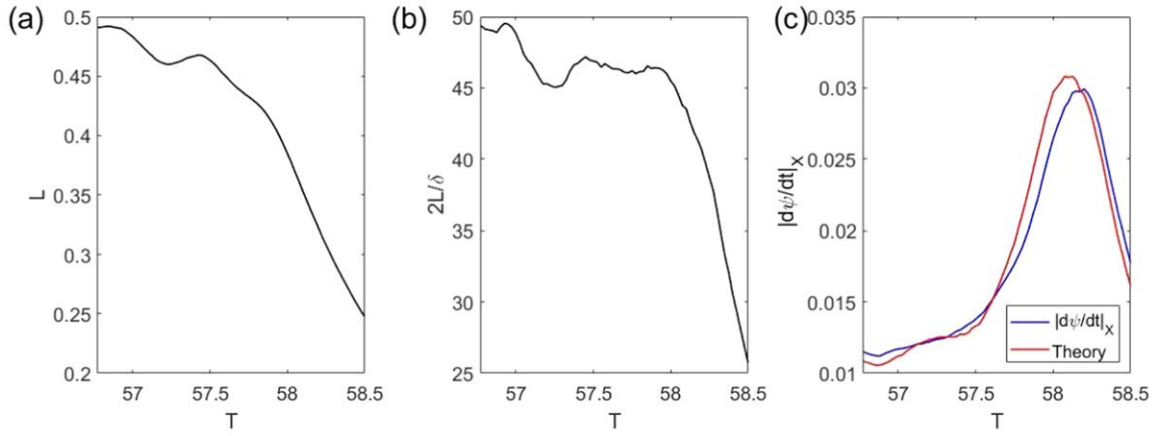

Figure 4. Time evolutions of (a) the half length L of the current sheet, (b) the aspect ratio $2L/\delta$ of the current sheet, and (c) the reconnection rates computed by the rate of change of the magnetic flux at the X-point $|d\psi/dt|_X$ and Equation (3) for Run D2.

region marked by a white cross with width δ and length $2L$. Figure 4 shows the time evolutions of the half length L of the current sheet, the aspect ratio $2L/\delta$, and the instantaneous reconnection rate. A relatively direct method for measuring the instantaneous reconnection rate is to compute the rate of change of the magnetic flux at the X-point $|d\psi/dt|_X$, which is shown in Figure 4(c). As can be seen, the local reconnection rate computed alternatively by applying the asymmetric current sheet model Equation (3) is in good agreement with the prediction by $|d\psi/dt|_X$.

A direct comparison between Run D2 with $\epsilon = 0.05$ and Run A2 with $\epsilon = 0$, both with the same Lundquist number, is made in Figure 5, including $\psi_{\max}(t)$, $|d\psi_{\max}(t)/dt|$, outflow speed and upstream magnetic field. As mentioned in Section 3, the outflow speed $v_{\rm out}$ and upstream magnetic field $B_{\rm upstream}$ are defined to be the largest v_y in the downstream region and the largest B_y in the upstream region, respectively. Although crudely, one observable feature in Figures 5(c) and (d) depicted by such an approximation is that both $v_{\rm out}$ and $B_{\rm upstream}$ are elevated in the presence of turbulence injection, which could contribute to the enhanced reconnection. This is consistent with the larger average $|d\psi_{\max}(t)/dt|$ for Run D2 than that for Run A2 in Figure 5(b). Summarizing these preliminary results at small Lundquist numbers without plasmoids, the externally

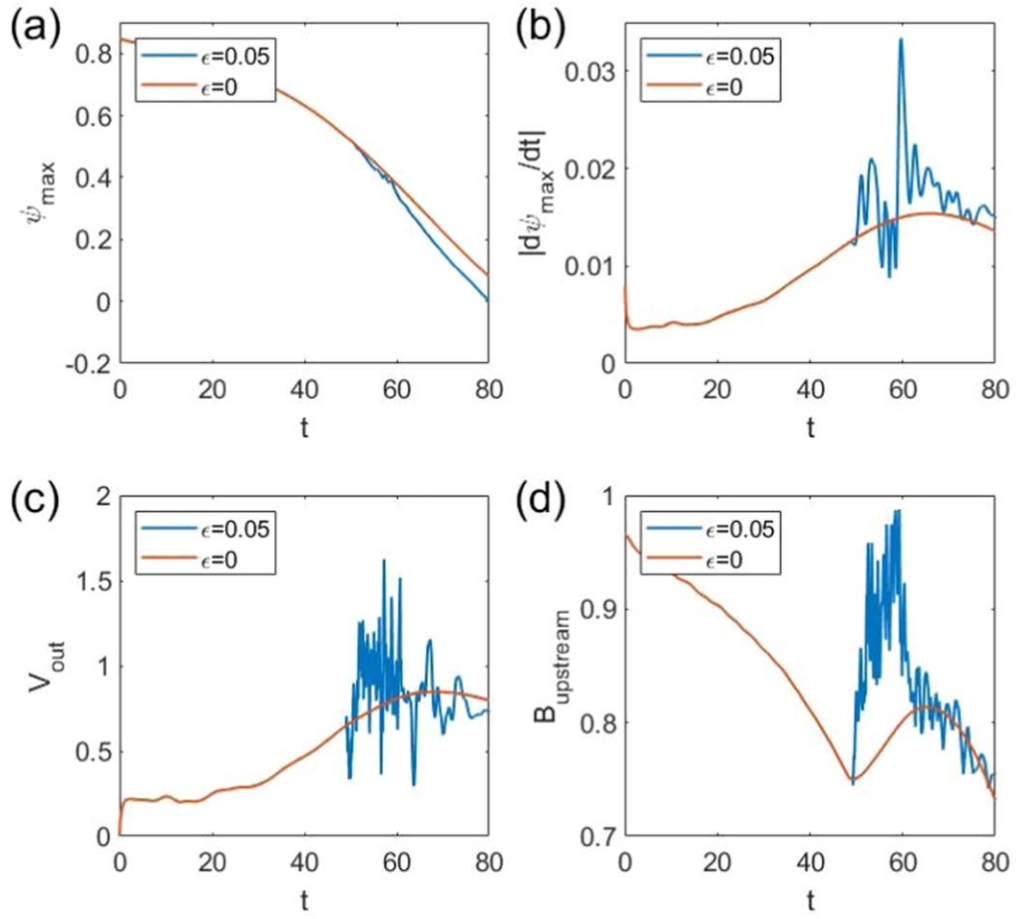

Figure 5. Time evolutions of (a) $\psi_{\max}(t)$, (b) absolute value of the local slope $|d\psi_{\max}(t)/dt|$, (c) the outward flow velocity $v_{\rm out}$, and (d) the upstream magnetic field $B_{\rm upstream}$ for Run D2 with $\epsilon = 0.05$ and Run A2 with $\epsilon = 0$.

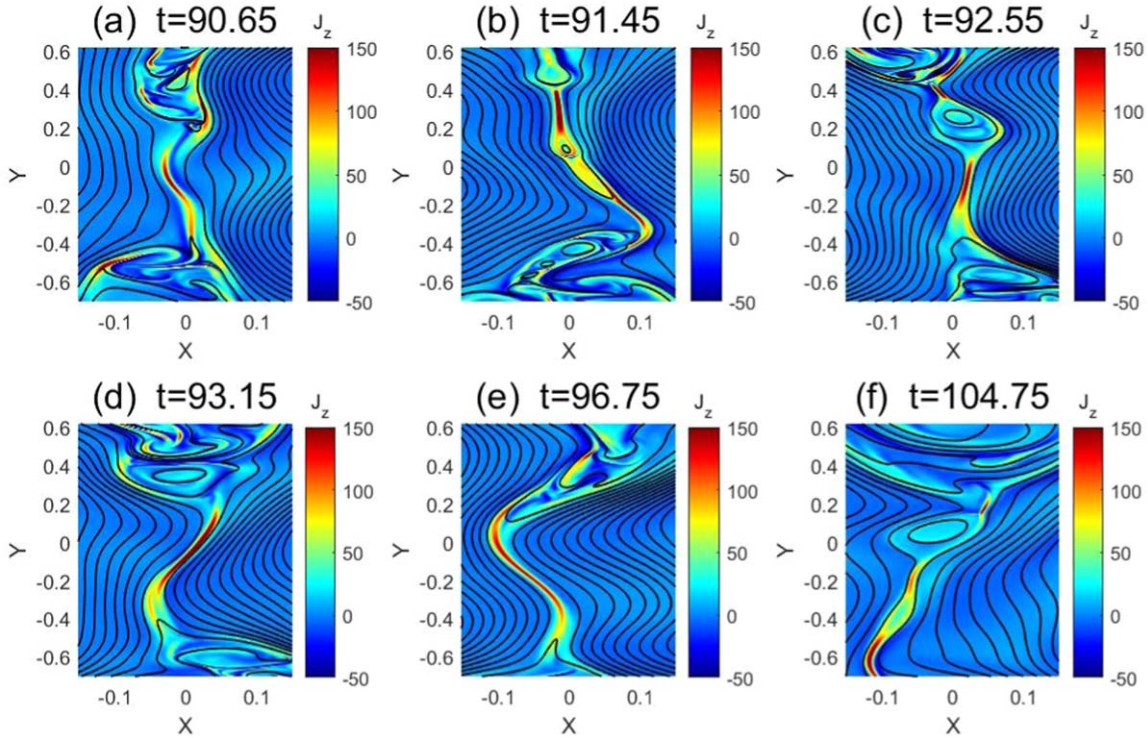

Figure 6. Configuration of current sheet together with contour lines (black solid lines) of magnetic potential for Run D3 at (a) $t = 90.65$, (b) $t = 91.45$, (c) $t = 92.55$, (d) $t = 93.15$, (e) $t = 96.75$, (f) $t = 104.75$.

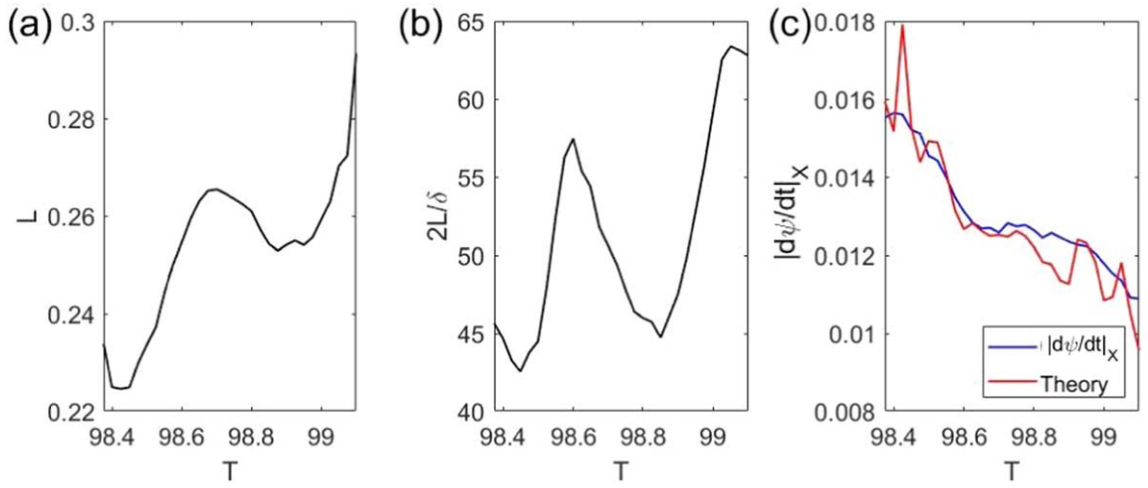

Figure 7. Time evolutions of (a) the half length L of the current sheet, (b) the aspect ratio $2L/\delta$ of the current sheet, and (c) the reconnection rates computed by the rate of change of the magnetic flux at the X-point $|d\psi/dt|_X$ and Equation (3) for Run D3.

driven turbulence could contribute to the conversion of magnetic energy to kinetic energy flowing out of the reconnection site and thus enhance the reconnection rate.

4.3. Reconnection Regime in Large S

Moving into the realm of the reconnection at large S, it is expected to be significantly different in character from the case at small S, at least for the plasmoid instability already explored. Figure 6 shows the time evolution of current sheet for Run D3, in which the current sheet is disordered. Moreover, there are plasmoids generated in the current sheet (see, for example, Figure 6(b)) and forming a hierarchy. The plasmoids are then expelled out of the current sheet together with the outflow (Figure 6(c)). After that, there will be a short period of time over which no plasmoids emerge in the current sheet (Figures 6(d) and (e)). The current sheet involves continual elongation and formation and expelling of plasmoids (Figure 6(f)). However, unlike Run D3, Run A3 (not shown here) at the same Lundquist number but without externally driven turbulence does not exhibit plasmoids. This infers a possible causality between the two phenomena. On the one hand, turbulence might facilitate the generation of plasmoids in the current sheet. On the other hand, similar to the cases at small S, both the outflow velocity and the upstream magnetic field increase due to the injected turbulence for Run D3 in a comparison with Run A3.

To identify the current sheet structure clearly, our analysis in Figure 7 will be limited in a short period of time over which there is no plasmoids in the current sheet, i.e., from $t = 98.3$ to $t = 100.0$ between Figures 6(e) and (f). As we can see, after the plasmoids are expelled, the current sheet is shorter than that in Run D2 (see Figure 4(a)). The current sheet is elongated gradually by the outflow of the current sheet (Figure 7(a)); so is the aspect ratio of the current sheet in Figure 7(b). As mentioned at the onset, the asymmetric current sheet model in Equation (3) does not accommodate the possible effect of plasmoids. Therefore, there is a reasonable agreement between the two estimations of the reconnection rate given in Figure 7(c). This is confirmed by more cases in Figure 8 at small Lundquist numbers (Figure 8(a)) and in the period without plasmoids in the current sheet at large Lundquist numbers (Figures 8(b)–(d)).

We conclude that when S is large, turbulence could show its effect on the reconnection rate enhancement in at least two ways: one is the contribution to the conversion of magnetic energy to kinetic energy flowing out of the reconnection, and the other is that turbulence might facilitate plasmoid formation. In this sense, both turbulence and plasmoids are operative to enhance the reconnection rate, while further work is needed to quantify the relative strength of the two processes.

4.4. Energy Conversion

One of the hallmarks of magnetic reconnection is magnetic energy conversion to flow and thermal energy. From Faraday's equation, we can obtain the governing equation of magnetic energy:

$$\frac{\partial E^m}{\partial t} = -\nabla \cdot (\boldsymbol{E} \times \boldsymbol{B}) - \boldsymbol{E} \cdot \boldsymbol{J},$$

where $E^m = B^2/2$ is the magnetic energy and $\boldsymbol{E}$ is the electric field calculated by the Ohm's law $\boldsymbol{E} = \eta \boldsymbol{J} - \boldsymbol{v} \times \boldsymbol{B}$. The energy release is through $\boldsymbol{E} \cdot \boldsymbol{J}$, the work done by the electric force, which has been investigated in particle acceleration (Dahlin et al. 2014, 2017; Li et al. 2015, 2017; Beresnyak 2016; Beresnyak & Li 2016; Lu et al. 2018).

Here we present quantitative studies of the energy release associated with the reconnection with different strengths of turbulence injection. As shown in Figure 9, the energy conversion through $\boldsymbol{E} \cdot \boldsymbol{J}$ in Run D3 is much larger than that in Run A3, which indicates that turbulence might strongly facilitate the local energy conversion. The energy-conversion rates averaged over the current sheet and downstream regions, marked, respectively, by the red and yellow rectangles in Figure 9(a), are $\langle \boldsymbol{E} \cdot \boldsymbol{J} \rangle_{\text{current sheet}} = 1.29$ and $\langle \boldsymbol{E} \cdot \boldsymbol{J} \rangle_{\text{downstream}} = 0.50$. Even when there is strong turbulence, the energy conversion preferentially occurs in the current sheet region.

In two dimensions, $\boldsymbol{E} \cdot \boldsymbol{J}$ can be decomposed as $\boldsymbol{E} \cdot \boldsymbol{J} = \boldsymbol{E} \cdot \left[\frac{\boldsymbol{B} \times (\boldsymbol{B} \cdot \nabla)\boldsymbol{B}}{B^2}\right] - \nabla\left(\frac{B^2}{2}\right) \cdot \frac{\boldsymbol{E} \times \boldsymbol{B}}{B^2} = \boldsymbol{E} \cdot \boldsymbol{J}_c - \nabla\left(\frac{B^2}{2}\right) \cdot \frac{\boldsymbol{E} \times \boldsymbol{B}}{B^2}$ (Yang et al. 2019), where the first term is the curvature drift acceleration and the second term can be combined with the Poynting flux $\nabla \cdot (\boldsymbol{E} \times \boldsymbol{B})$, which is not of interest in this work. Alternatively, $\boldsymbol{E} \cdot \boldsymbol{J}$ can be decomposed as $\boldsymbol{E} \cdot \boldsymbol{J} = \eta J^2 - (\boldsymbol{v} \times \boldsymbol{B}) \cdot \boldsymbol{J}$, where the two terms refer to the dissipation by

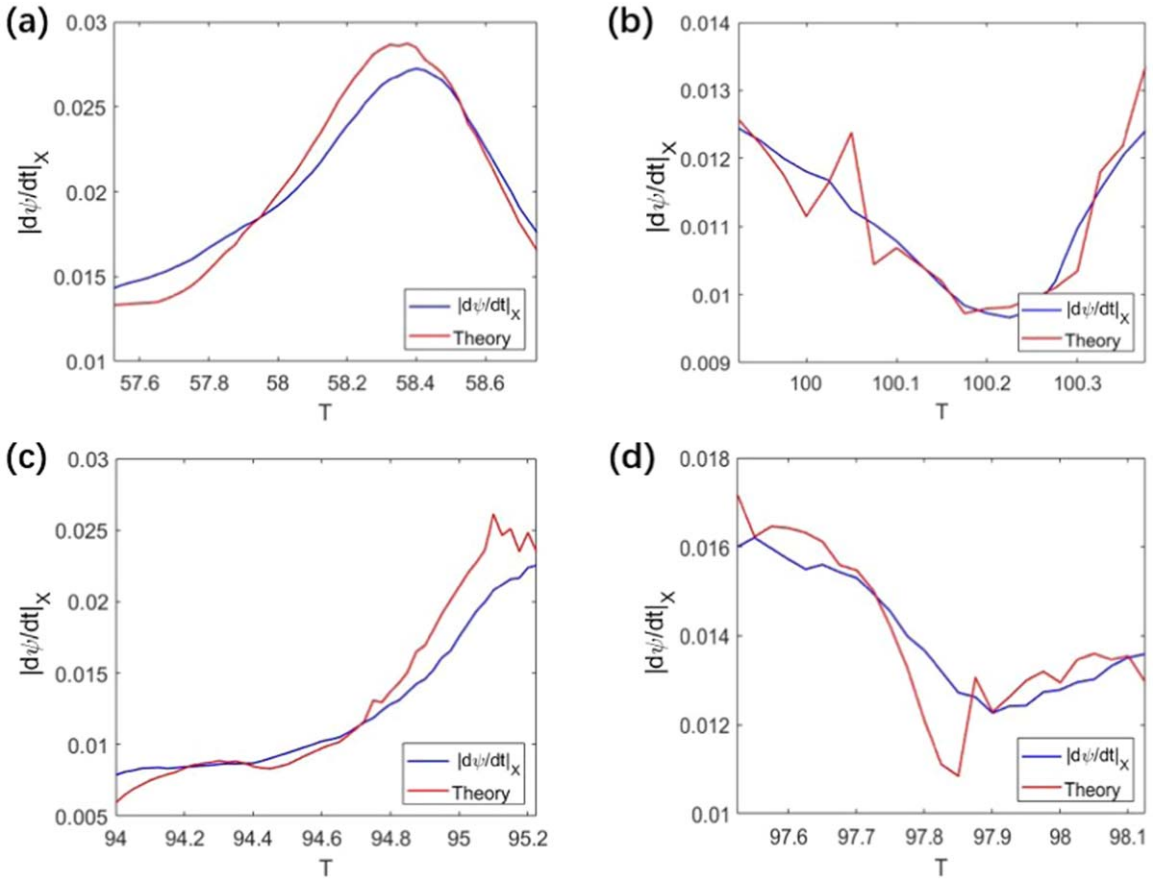

Figure 8. Comparison between the reconnection rates computed by the rate of change of the magnetic flux at the X-point $|d\psi/dt|_X$ and Equation (3) for (a) Run C2, (b) Run D3, (c) Run E3, and (d) Run E4.

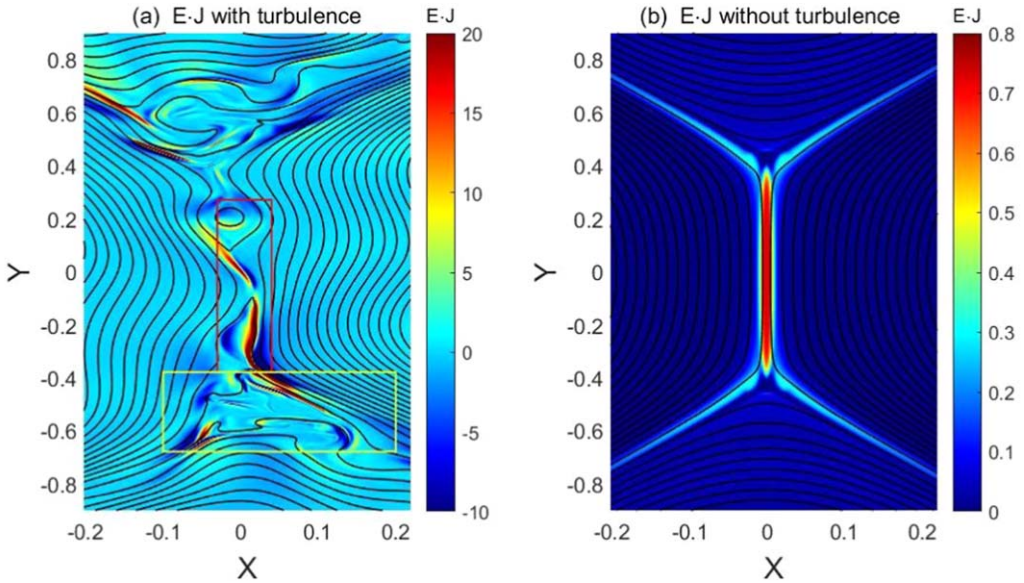

Figure 9. Contour maps of $\boldsymbol{E}\cdot\boldsymbol{J}$ together with contour lines (black solid lines) of magnetic potential at $t = 71.5$ for (a) Run D3 with turbulence injection and (b) Run A3 without turbulence injection. The red and yellow rectangles in (a) indicate the current sheet and downstream regions, respectively.

ohmic and nonohmic heating, respectively. Figures 10 and 11 show different components of $\boldsymbol{E}\cdot\boldsymbol{J}$ for Run A3 and Run D3. In Run A3 (see Figures 10(c) and (d)), the major contributor to $\boldsymbol{E}\cdot\boldsymbol{J}$ is the ohmic heating ηJ^2. In contrast, in Run D3 with turbulence injection (see Figures 11(c) and (d)), the nonohmic heating $-(\boldsymbol{v}\times\boldsymbol{B})\cdot\boldsymbol{J}$ makes a major contribution. Note that the nonohmic heating is very small at the X-point because of the weakness of the magnetic field there. Previous studies on magnetic reconnection emphasize the prominence of curvature drift acceleration in reconnection exhausts, at ends of contracting magnetic islands and in island merging regions (Dahlin et al. 2014, 2017; Li et al. 2015, 2017; Beresnyak 2016; Lu et al.

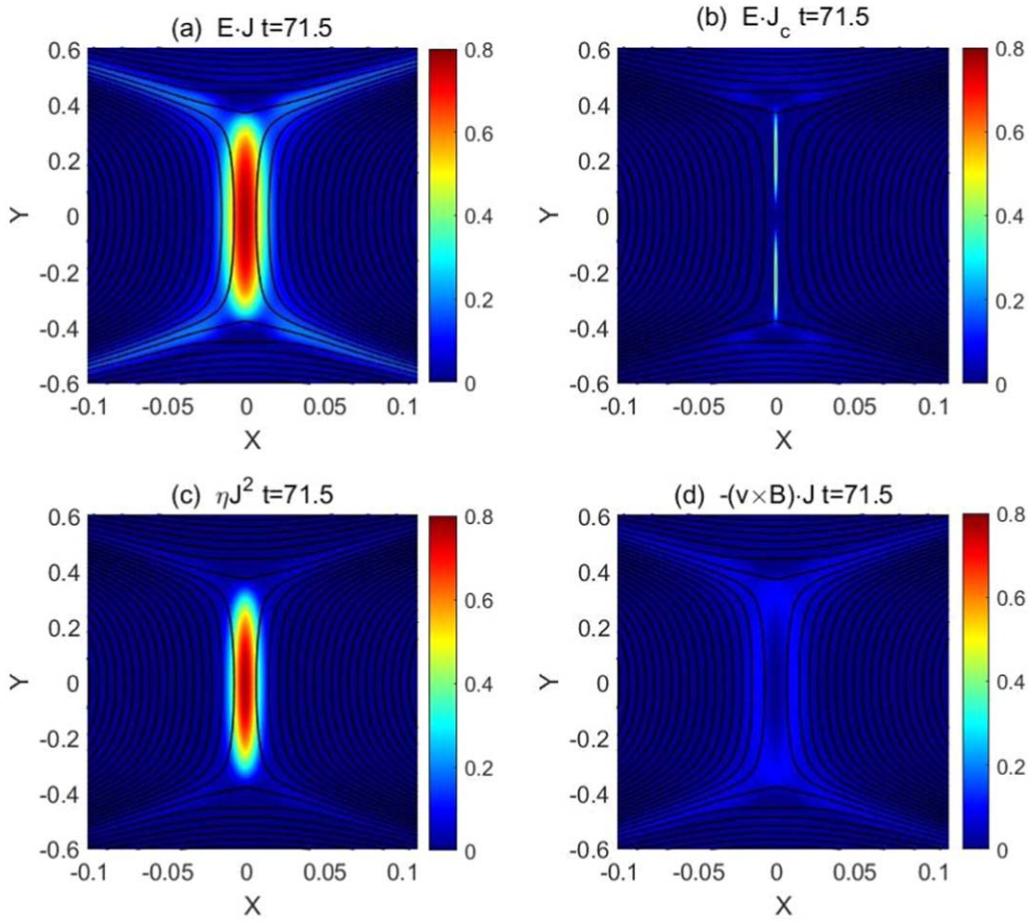

Figure 10. Energy-conversion rate due to different components of $\boldsymbol{E} \cdot \boldsymbol{J}$ for Run A3 at $t = 71.5$: (a) $\boldsymbol{E} \cdot \boldsymbol{J}$, (b) curvature drift term $\boldsymbol{E} \cdot \boldsymbol{J}_c$, (c) ohmic heating $\eta \boldsymbol{J}^2$, and (d) nonohmic heating $-(\boldsymbol{v} \times \boldsymbol{B}) \cdot \boldsymbol{J}$. Contour lines of magnetic potential are plotted as black solid lines.

2018). The importance of this process also emerges here, where the high curvature drift acceleration occurs at the ends of the current sheet in Figure 10(b) and around the rims of magnetic islands in Figure 11(b).

4.5. Stability Analysis of Kelvin–Helmholtz Instabilities

The Kelvin–Helmholtz (K-H) instability is an MHD shear-driven instability frequently observed in solar system plasmas (Hones et al. 1981; Chen et al. 1997; Otto & Fairfield 2000; Hasegawa et al. 2004; Foullon et al. 2008; Huang et al. 2015, 2017; Eriksson et al. 2016; Ruffolo et al. 2020; Kieokaew et al. 2021). Based on the linear theory of Chandrasekhar (1961), the K-H instability onset condition for an infinitely thin shear layer requires $(\Delta v)^2 > 2(v_{A1}^2 + v_{A2}^2)$, where v_{A1} and v_{A2} are the Alfvén velocity on either side of the shear layer. In this sense, the K-H instability may be found in the outflow region in the magnetic reconnection, where the magnetic field is generally weak, making the conditions to meet the K-H instability criterion easier (see, for example, Figure 1 in Loureiro et al. 2013).

Despite the theoretical criterion, it is not easy to resolve directly the signatures of K-H waves in two-dimensional MHD magnetic reconnection. One possible reason is that it requires a very high Lundquist number to allow a shear layer to be unstable to K-H instability (Loureiro & Uzdensky 2016). Here, we report the local configuration of a shear layer in the downstream region of magnetic reconnection that might be unstable to the K-H instability. Contour lines of magnetic potential and velocity vectors for Run D3 are plotted on the top of the color map of vorticity in Figure 12(a). One can see the directional change of the velocity and magnetic fields across the shear layer. Figure 12(b) illustrates that there is strong energy dissipation in the proximity of the high vorticity region. To test whether the observed local conditions satisfy the K-H instability onset criterion, we show velocity and Alfvén speed profiles in Figure 12(c). To simplify the configuration of the observed shear layer, we only consider the y-direction components since the x-direction components are small. The velocity shear is clearly seen in the v_y component. To mark the shear layer, we define the two positions indicated by red dashed lines in Figure 12(c) as the two sides of the shear layer, which are local minimum and maximum of v_y, respectively. Then the local configuration is simplified as a shear layer with $\Delta v_y \approx 3.0$, $|v_{A1}| \approx 0.7$ and $|v_{A2}| \approx 0.0$, and the K-H growth rate of a wave mode $\boldsymbol{k}$ from this simplified configuration is $\gamma/k \approx 1.4$. This means that according to the linear theory analysis of an infinitely thin shear layer, the observed conditions are unstable to the K-H instability.

Note that a shear layer of zero thickness is unrealistic and it is of great importance to treat the finite thickness of the shear layer, as shown in Figure 12(c). The linear theory of a finite

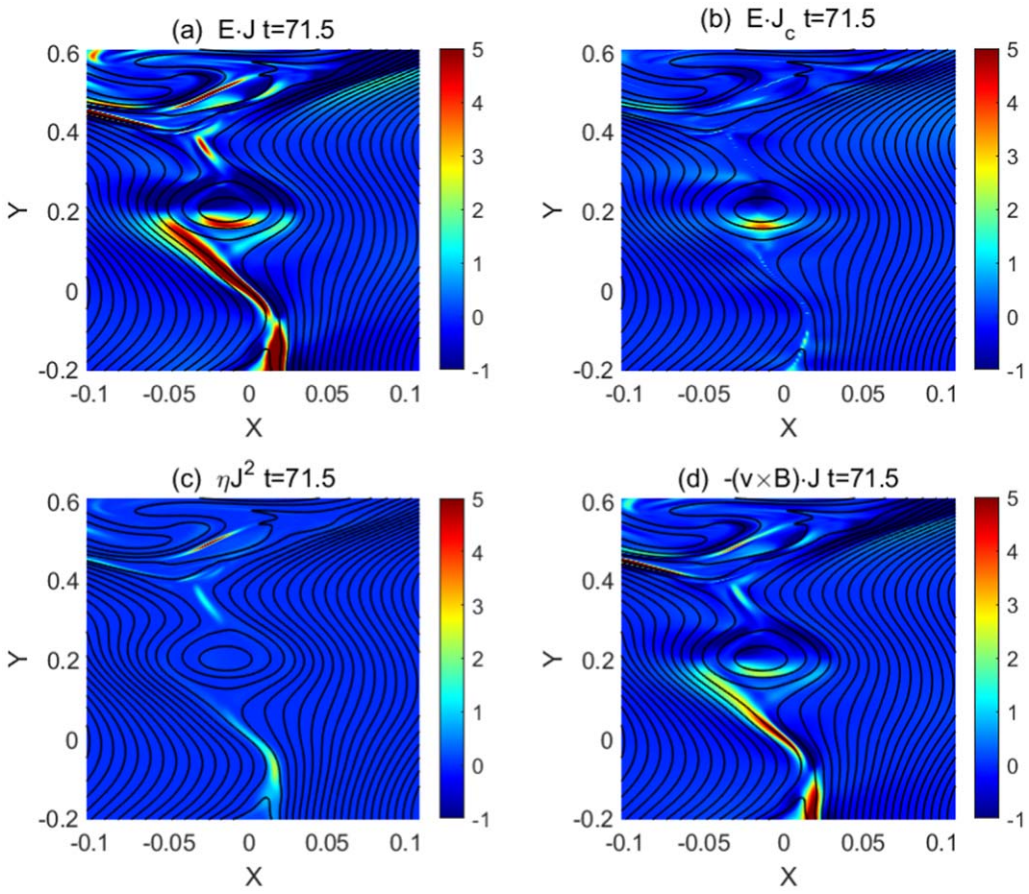

Figure 11. Energy-conversion rate due to different components of $\boldsymbol{E}\cdot\boldsymbol{J}$ for Run D3 at $t = 71.5$: (a) $\boldsymbol{E}\cdot\boldsymbol{J}$, (b) curvature drift term $\boldsymbol{E}\cdot\boldsymbol{J}_c$, (c) ohmic heating $\eta\boldsymbol{J}^2$, and (d) nonohmic heating $-(\boldsymbol{v}\times\boldsymbol{B})\cdot\boldsymbol{J}$. Contour lines of magnetic potential are plotted as black solid lines.

thickness shear layer by Miura & Pritchett (1982) predicts that the fastest growing modes occur for $k\Delta \sim 0.5$–1.0, where Δ is the thickness of the shear layer. Using the estimated shear layer thickness $\Delta \approx 0.04$, the fastest growing mode should have the wavelength $\lambda = 2\pi/k \sim 0.3$–$0.5$ and the corresponding growth rate $\gamma \sim 4$–15. This wavelength is comparable to the characteristic spatial scale of the downstream region, which indicates that there might not be ample room for the shear layer to grow into a nonlinear stage where multiple rolled-up K-H vortices on both sides of the velocity profile clearly form. Meanwhile, as in comparison with the time $1/\gamma$ obtained above, the turbulence could impact the local geometry significantly in a shorter time, again suggesting that the configurations of the velocity and magnetic field at the time of observation are not representative of pure K-H waves.

In brief, the linear theory analysis is in favor of the possible development of K-H instability from this shear layer configuration. However, the development of K-H waves and the procedure for tracking the evolvement of this shear layer in our simulations are challenging, as many issues in reality may arise.

5. Discussion and Conclusions

In this paper, we analyzed the reconnection regime for two-dimensional MHD turbulent reconnection under different Lundquist numbers S. We found that when S is small (smaller than about 10^4, while the exact value may vary for different turbulent strength and simulation configurations), there is no plasmoids within the turbulent current sheet. The reconnection rate can be described reasonably by the reconnection rate equations for asymmetric current sheet Equations (3)–(4). Meanwhile, the external energy input from turbulent forcing contributes to the conversion of magnetic energy to kinetic energy flowing out of the reconnection site, giving rise to larger outflow velocity and upstream magnetic field. In addition to this effect, turbulence could facilitate the generation of plasmoids when S is large. Although the results have been reported in favor of the effect of turbulence and plasmoids on magnetic reconnection, the relative strength of the two effects remains to be an open issue. Turbulence has an impact on the formation of plasmoids that in turn affect turbulent energy spectra (Dong et al. 2018). It is therefore hard to implement any present theories to elucidate or extract individual contributions of turbulence and plasmoids.

The energy conversion around the current sheet has also been studied in detail. The magnetic energy-conversion rate in a turbulent current sheet is much larger than that in a Sweet–Parker current sheet. By decomposing the energy-conversion term $\boldsymbol{E}\cdot\boldsymbol{J}$ into ohmic and nonohmic parts, we find that the major conversion for a turbulent current sheet is through the nonohmic part, while the ohmic part contributes most for a Sweet–Parker current sheet. The curvature drift term concentrates around the rims of magnetic islands. A shear layer is observed in the downstream region of the turbulent current sheet, where weak magnetic field contributes to the possible development of K-H waves. Using the linear theory analysis,

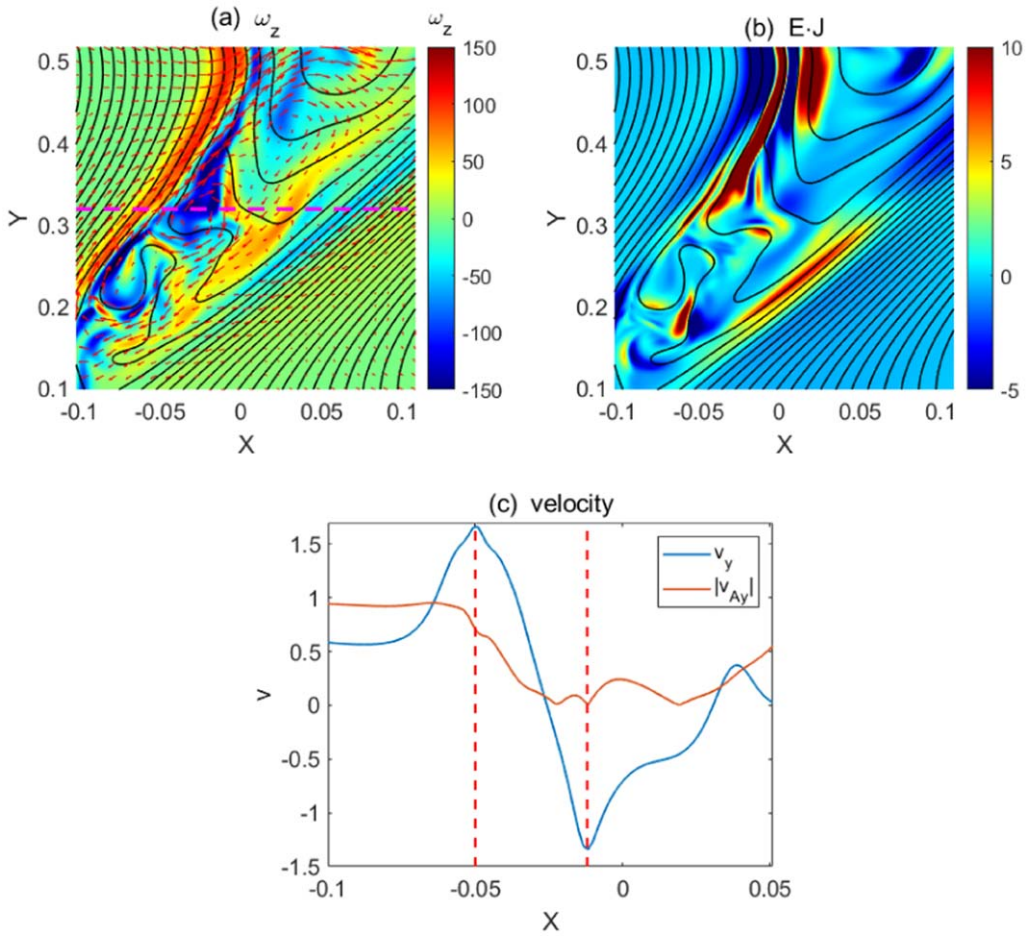

Figure 12. Local configuration of a shear layer in the downstream region of magnetic reconnection for Run D3 at $t = 78.5$. (a) Contour map of the out-of-plane vorticity together with contour lines (black solid lines) of magnetic potential and velocity vectors (red vectors). (b) Contour map of the magnetic energy release rate $\boldsymbol{E} \cdot \boldsymbol{J}$. (c) Velocity and Alfvén speed profiles along the pink dashed line in (a).

the local conditions satisfy the K-H instability onset criterion, but no clear signatures of fully developed K-H waves are found in our simulations. The lack of these signatures may be due to the complicated configuration triggered by turbulence and the limited spatial and temporal scales.

Shown in Figure 13 is the dependence of the global reconnection rate (as shown in Figure 2(a)) on the power of turbulence ε. The global reconnection rate increases with ε in a power-law scaling $E_{\rm Global} \sim \varepsilon^{0.22}$. Although the power-law exponent does not show apparent discrepancy from those in Loureiro et al. (2009) and Kulpa-Dybeł et al. (2010) for the two-dimensional case, this is significantly shallower than the LV99 prediction of $\varepsilon^{1/2}$ scaling for the three-dimensional case (Kowal et al. 2009). It is natural to imagine that the two-dimensional description could be significantly different from its three-dimensional counterpart, thus leading to rather different nature of reconnection (Kulpa-Dybeł et al. 2010; Beresnyak 2016) and plasmoid instability (Huang & Bhattacharjee 2016). That the real system is three-dimensional and two-dimensional is not the answer to the final problem. We might miss some effects in such a limit. We propose this as a starting point because it appears relatively easy to figure out the configuration of reconnection and energy release without the third dimension. In this paper, we also avoid the complexity of the compression in low-β plasmas, where the reconnection site will be dominated by shocks and shock-related structures and plasma compression is significant (Zenitani & Miyoshi 2020). Based on the results

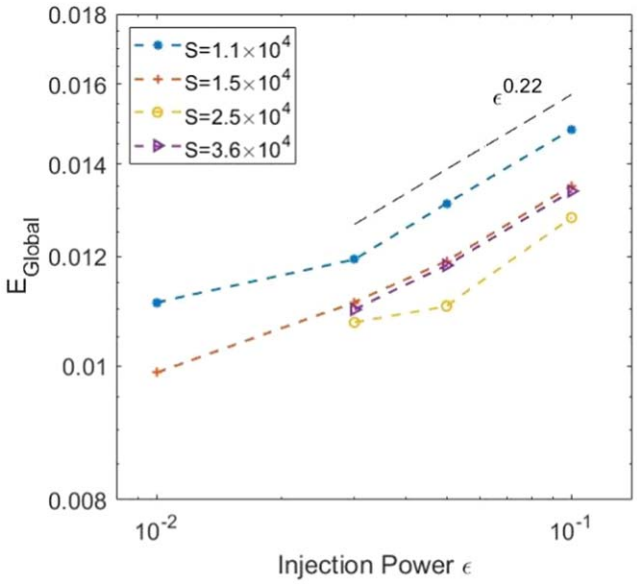

Figure 13. The global reconnection rate as a function of the power of turbulence for some Lundquist numbers S. A power law $E_{\rm Global} \sim \varepsilon^{0.22}$ is plotted as a reference.

for the incompressible model here in the high-β regime, further work is needed on this path to include compression effects when the plasma β is extremely low. We also keep in mind that our

simulations have many limitations (e.g., unity Prandtl number (i.e., the effect of viscosity), periodic boundary condition, etc), which we defer to future work.

This work is supported by the NSFC grants 41774169, Key Research Program of Frontier Sciences, CAS (QYZDJ-SSWDQC010), and the Strategic Priority Research Program of Chinese Academy of Sciences, grant No. XDB 41000000. Y. Y. is supported by grant No. 11902138 from the National Natural Science Foundation of China.

Appendix

The asymmetric reconnection model was first given in Cassak & Shay (2007). The "steady-state" assumption was made to arrive at Equation (3) (i.e., Equation (35) in Cassak & Shay 2007). All simulations in this paper were driven by external turbulence. We make a detailed treatment of terms in MHD equations for the justification of the "steady-state" assumption.

First, the time derivative of density $\partial\rho/\partial t$ is zero since the density is a constant in our simulations. Second, the turbulent velocity is set to be a random variable and its spatial average should be vanishing. There is no need to consider the time derivative of momentum $\partial\rho\boldsymbol{v}/\partial t$. The remaining is the time derivative of magnetic field $\partial\boldsymbol{B}/\partial t$ and the time derivative of total energy: $\partial E_{\rm total}/\partial t$.

Faraday's law gives:

$$\frac{\partial \boldsymbol{B}}{\partial t} = -\nabla \times \boldsymbol{E}. \tag{A1}$$

Ohm's law gives

$$\boldsymbol{E} = \eta \boldsymbol{j} - \boldsymbol{v} \times \boldsymbol{B}. \tag{A2}$$

Integrating Equation (A1) over the ABXW domain in Figure A1 and using Stokes' theorem and the fact that $j = \frac{1}{\mu_0}\nabla \times \boldsymbol{B} \cdot \hat{z}$, we obtain

$$\frac{\partial B_1}{\partial t}\delta_1 L + v_1 B_1 L \sim \eta j L \sim \frac{\eta}{\mu_0}\frac{B_1}{\delta_1}L, \tag{A3}$$

where we use the fact that the magnetic field is zero along the X line. Here we take Run D4 as an example to estimate the ratio of the first and second terms on the left-hand side of Equation (A3). We then obtain: $\left|\frac{\partial B_1}{\partial t}\frac{1}{B_2}\frac{\delta_1}{v_1}\right|_{\rm max} \sim$ O(0.02) $\ll$ O(1), where the maximum is taken over $t =$ 90–100, after the turbulence has developed in Run D4. It is reasonable to neglect the time derivative of magnetic field $\partial\boldsymbol{B}/\partial t$.

The energy equation evaluated for the same domain gives

$$L\left(\frac{B_1^2}{2\mu_0} + \frac{B_2^2}{2\mu_0}\right) + 2L\delta\frac{\partial E_{\rm total}}{\partial t} \sim 2\delta\left(\frac{1}{2}\rho_{\rm out}v_{\rm out}^2\right)v_{\rm out}, \tag{A4}$$

which is slightly different from Equation (11) in Cassak & Shay (2007). Similarly, we can estimate the ratio of the first and second terms on the left-hand side of Equation (A4): $\left|2\delta\frac{\partial E_{\rm total}}{\partial t}\Big/\left(\frac{B_1^2}{2\mu_0} + \frac{B_2^2}{2\mu_0}\right)\right|_{\rm max} \sim$ O(0.05) $\ll$ O(1). Therefore, the time derivative of total energy $\partial E_{\rm total}/\partial t$ is negligible, as well.

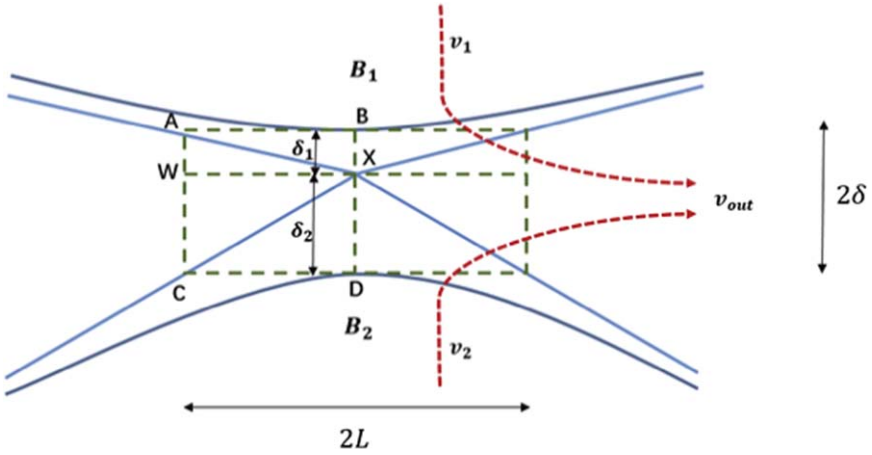

Figure A1. Schematic diagram of the dissipation region in an asymmetric reconnection.

ORCID iDs

Haomin Sun https://orcid.org/0000-0001-7403-6450
Yan Yang https://orcid.org/0000-0003-2965-7906
Quanming Lu https://orcid.org/0000-0003-3041-2682
San Lu https://orcid.org/0000-0003-2248-5072
Minping Wan https://orcid.org/0000-0001-5891-9579
Rongsheng Wang https://orcid.org/0000-0002-9511-7660

References

Bellan, P. M. 2004, Fundamentals of Plasma Physics (Cambridge: Cambridge Univ. Press)
Beresnyak, A. 2016, ApJ, 834, 47
Beresnyak, A., & Li, H. 2016, ApJ, 819, 90
Bhattacharjee, A., Huang, Y.-M., Yang, H., & Rogers, B. 2009, POP, 16, 112102
Birn, J., Borovsky, J. E., & Hesse, M. 2012, POP, 19, 082109
Biskamp, D. 1986, POF, 29, 1520
Cassak, P. A., & Shay, M. A. 2007, POP, 14, 102114
Cassak, P. A., Shay, M. A., & Drake, J. F. 2009, POP, 16, 120702
Chandrasekhar, S. 1961, Hydrodynamic and Hydromagnetic Stability (Oxford: Clarendon Press)
Che, H., Drake, J. F., & Swisdak, M. 2011, Natur, 474, 184
Chen, Q., Otto, A., & Lee, L. C. 1997, JGR, 102, 151
Chhiber, R., Chasapis, A., Bandyopadhyay, R., et al. 2018, JGR, 123, 9941
Ciaravella, A., & Raymond, J. C. 2008, ApJ, 686, 1372
Dahlin, J., Drake, J., & Swisdak, M. 2014, POP, 21, 092304
Dahlin, J., Drake, J., & Swisdak, M. 2017, POP, 24, 092110
Daughton, W., Nakamura, T. K. M., Karimabadi, H., et al. 2014, POP, 21, 052307
Daughton, W., Roytershteyn, V., Albright, B. J., et al. 2009, PRL, 103, 065004
Daughton, W., Roytershteyn, V., Karimabadi, H., et al. 2011, NatPh, 7, 539
Dong, C. F., Wang, L., Huang, Y., et al. 2018, PRL, 121, 165101
Drake, F., Swisdak, M., Che, H., et al. 2006, Natur, 443, 553
Drury, L. O. C. 2012, MNRAS, 422, 2474
Dungey, J. 1953, PMag, 44, 725
Egedal, J., Øieroset, M., Fox, W., et al. 2005, PRL, 94, 025006
Eriksson, S., Lavraud, B., Wilder, F. D., et al. 2016, GRL, 43, 5606
Eriksson, S., Vaivads, A., Graham, D. B., et al. 2018, GRL, 45, 8081
Eyink, G. L. 2015, ApJ, 807, 137
Fan, Q., Feng, X., & Xiang, C. 2004, POP, 11, 5605
Foullon, C., Farrugia, C., Fazakerley, A., et al. 2008, JGRA, 113, A11203
Franci, L., Cerri, S. S., Califano, F., et al. 2017, ApJL, 850, L16
Goldreich, P., & Sridhar, S. 1995, ApJ, 438, 763
Gosling, J. T. 2007, ApJL, 671, L73
Haggerty, C. C., Parashar, T. N., Matthaeus, W. H., et al. 2017, POP, 24, 102308
Hasegawa, H., Fujimoto, M., Phan, T.-D., et al. 2004, Natur, 430, 755
Hesse, M., & Schindler, K. 1988, JGR, 93, 5559
Hones, E. W., Birn, J., Bame, S. J., et al. 1981, JGR, 86, 814
Huang, C., Lu, Q., Guo, F., et al. 2015, GRL, 42, 7282
Huang, C., Lu, Q., Wang, R., et al. 2017, ApJ, 835, 245
Huang, Y.-M., & Bhattacharjee, A. 2010, POP, 17, 062104
Huang, Y.-M., & Bhattacharjee, A. 2013, POP, 20, 055702
Huang, Y.-M., & Bhattacharjee, A. 2016, ApJ, 818, 20
Karimabadi, H., & Lazarian, A. 2013, POP, 20, 112102
Karimabadi, H., Roytershteyn, V., Wan, M., et al. 2013, POP, 20, 012303
Kieokaew, R., Lavraud, B., Yang, Y., et al. 2021, A&A, 656, A12
Kowal, G., Lazarian, A., Vishniac, E. T., et al. 2009, ApJ, 700, 63
Kowal, G., Lazarian, A., Vishniac, E. T., et al. 2012, NPG, 19, 297
Kowal, G., Falceta-Gonçalves, D. A., Lazarian, A., et al. 2017, ApJ, 838, 91
Kulpa-Dybeł, K., Kowal, G., Otmianowska-Mazur, K., et al. 2010, A&A, 514, A26
Lapenta, G. 2008, PRL, 100, 235001
Lazarian, A., Eyink, G., Vishniac, E., et al. 2015, RSPTA, 373, 20140144
Lazarian, A., & Vishniac, E. T. 1999, ApJ, 517, 701
Li, X., Guo, F., Li, H., et al. 2015, ApJL, 811, L24
Li, X., Guo, F., Li, H., et al. 2017, ApJ, 843, 21
Li, X., Guo, F., Li, H., & Li, S. 2018, ApJ, 866, 4
Liu, W., Petrosian, V., Dennis, B. R., et al. 2008, ApJ, 676, 704
Loureiro, N. F., Cowley, S. C., Dorland, W. D., et al. 2005, PRL, 95, 235003
Loureiro, N. F., Samtaney, R., Schekochihin, A. A., et al. 2012, POP, 19, 042303
Loureiro, N. F., Schekochihin, A. A., & Cowley, S. C. 2007, POP, 14, 100703
Loureiro, N. F., Schekochihin, A. A., & Uzdensky, D. A. 2013, PRE, 87, 013102
Loureiro, N. F., & Uzdensky, D. A. 2016, PPCF, 58, 014021
Loureiro, N. F., Uzdensky, D. A., Schekochihin, A. A., et al. 2009, MNRAS, 399, L146
Lu, Q., Wang, H., Huang, K., Wang, R., & Wang, S. 2018, POP, 25, 072126
Malyshkin, L. M., Linde, T., & Kulsrud, R. M. 2005, POP, 12, 102902
Matthaeus, W. H., & Lamkin, S. L. 1985, POF, 28, 303
Matthaeus, W. H., & Lamkin, S. L. 1986, POF, 29, 2513
Miura, A., & Pritchett, P. L. 1982, JGR, 87, 7431
Montag, P., Egedal, J., & Lichko, E. 2017, POP, 24, 062906
Nagai, T., Shinohara, I., Fujimoto, M., et al. 2003, JGR, 108, 1357
Øieroset, M., Lin, R. P., Phan, T. D., et al. 2002, PRL, 89, 195001
Ono, Y., Tanabe, H., Yamada, T., et al. 2015, POP, 22, 055708
Osman, K. T., Matthaeus, W. H., Gosling, J. T., et al. 2014, PRL, 112, 215002
Otto, A., & Fairfield, D. H. 2000, JGRA, 105, 21175
Parker, E. N. 1957, JGR, 62, 509
Parker, E. N. 1973, ApJ, 180, 247
Petschek, H. E. 1964, in AAS-NASA Symp., The Physics of Solar Flares, ed. W. N. Hess (Washington, DC: NASA), 425
Phan, T. D., Eastwood, J. P., Shay, M. A., et al. 2018, Natur, 557, 202
Pope, S. B. 2004, Turbulent Flows (Cambridge: Cambridge Univ. Press)
Provornikova, E., Laming, J. M., & Lukin, V. S. 2016, ApJ, 825, 55
Pucci, F., Matthaeus, W. H., Chasapis, A., et al. 2018, ApJ, 867, 10
Retinò, A., Sundkvist, D., Vaivads, A., et al. 2007, NatPh, 3, 236
Ruffolo, D., Matthaeus, W. H., Chhiber, R., et al. 2020, ApJ, 902, 94
Samtaney, R., Loureiro, N. F., Uzdensky, D. A., et al. 2009, PRL, 103, 105004
Servidio, S., Matthaeus, W. H., Shay, M. A., et al. 2010, POP, 17, 032315
Servidio, S., Matthaeus, W. H., Shay, M. A., et al. 2009, PRL, 102, 115003
Shay, M. A., Haggerty, C. C., Matthaeus, W. H., et al. 2018, POP, 25, 012304
Smith, D., Ghosh, S., Dmitruk, P., et al. 2004, GRL, 31, L02805
Sonnerup, B. U. Ö. 1974, JGR, 79, 1546
Stawarz, J. E., Eastwood, J. P., Phan, T. D., et al. 2019, ApJL, 877, L37
Su, Y., Astrid, M. V., Gordon, D. H., et al. 2013, NatPh, 9, 489
Sundkvist, D., Retinò, A., Vaivads, A., et al. 2007, PRL, 99, 025004
Sweet, P. A. 1958, in IAU Symp. 6, Electromagnetic Phenomena in Cosmical Physics, ed. B. Lehnert (Cambridge: Cambridge Univ. Press), 123
Sych, R., Nakariakov, V. M., Karlicky, M., et al. 2009, A&A, 505, 791
Takasao, S., Ayumi, A., Hiroaki, I., et al. 2012, ApJL, 745, L6
Uzdensky, D. A. 2011, SSRv, 160, 45
Uzdensky, D. A., & Kulsrud, R. M. 2000, POP, 7, 4018
Uzdensky, D. A., Loureiro, N. F., & Schekochihin, A. A. 2010, PRL, 105, 235002
Vörös, Z., Yordanova, E., Varsani, A., et al. 2017, JGRA, 122, 11442
Wang, R. S., Lu, Q. M., Nakamura, R., et al. 2016, NPHY, 12, 263
Wang, Y., Yuan, X., Hu, D., et al. 2021, JGR, 126, e29000
Yamada, M., Kulsrud, R., & Ji, H. 2010, RvMP, 82, 603
Yamada, M., Levinton, F. M., Pomphrey, N., et al. 1994, POP, 1, 3269
Yang, L., Li, Hui, Guo, F., et al. 2020, ApJL, 901, L22
Yang, Y., Wan, M., Matthaeus, W. H., et al. 2019, POP, 26, 072306
Yokoyama, T., Akita, K., Morimoto, T., et al. 2001, ApJL, 546, L69
Yordanova, E., Vörös, Z., Varsani, A., et al. 2016, GRL, 43, 5969
Zank, G. L., Roux, L., Webb, J. A., et al. 2014, ApJ, 797, 28
Zenitani, S., & Miyoshi, T. 2020, ApJL, 894, L7
Zhdankin, V., Uzdensky, D. A., Perez, J. C., et al. 2013, ApJ, 771, 124
Zweibel, E. G., & Yamada, M. 2009, ARAA, 47, 291